First observation of off-season lee wave formation over the Arsia Mons in Mars

Anirban Guha[1] and Jyotirmoy Kalita[1]

[1]Tripura University

November 22, 2022

Abstract

We report the first observation of the largest Martian lee wave and its atmospheric characteristics over Arsia Mons Elongated Cloud (AMEC). We analyze the wavelength, the cloud's height, and wind speed from the lee wave structure. The estimated wind speed is 86±4.9 m/s, with a wavelength of 60± 0.3 km at the height of 55±7 km. This is the largest lee wave structure that appears during dust storm season (Ls=230 to Ls=300) and strongly contributes to the planet's Aerosol Optical Depth (AOD) level. Estimated AOD varies from 1.7 (Red channel) to 2.5 (Blue channel), and indicates the maximum contribution from the water ice crystal. The estimated angstrom exponent (α) value signifies coarse mode particle presence in the cloud with an effective radius of 3.2μm. The presence of water ice crystal contributes to the albedo level's increment to 0.8 and signifies the formation temperature for AMEC to be around 190 K.

First observation of off-season lee wave formation over the Arsia Mons in Mars

J Kalita and A Guha*

Department of Physics, Tripura University, Suryamaninagar, Tripura-799022, India

* Corresponding author: anirban1001@yahoo.com

Key Points:

- Off-season largest wavelength lee wave cloud structure is observed over the Southwestern slope of Arsia Mons.
- High westerlies and the low northern wind shear are responsible for the shape of the entire cloud structure.
- Solar radiation contributes to the deep convection process that raises the cloud into the Martian Atmosphere's mesosphere.

Abstract

We report the first observation of the largest Martian lee wave and its atmospheric characteristics over Arsia Mons Elongated Cloud (AMEC). We analyze the wavelength, the cloud's height, and wind speed from the lee wave structure. The estimated wind speed is 86±4.9 m/s, with a wavelength of 60± 0.3 km at the height of 55±7 km. This is the largest lee wave structure that appears during dust storm season (Ls=230 to Ls=300) and strongly contributes to the planet's Aerosol Optical Depth (AOD) level. Estimated AOD varies from 1.7 (Red channel) to 2.5 (Blue channel), and indicates the maximum contribution from the water ice crystal. The estimated angstrom exponent (α) value signifies coarse mode particle presence in the cloud with an effective radius of 3.2μm. The presence of water ice crystal contributes to the albedo level's increment to 0.8 and signifies the formation temperature for AMEC to be around 190 K.

Plain Language Summary

An elongated off-season cloud was reported near Arsia Mons by Bernal et al., 2020. This extended cloud is also captured by Mars Color Camera (MCC) during 2014 and 2015. In our present study, we considered a total of four events (Limb view and Nadir view) from ISRO-MOM data to report the atmospheric characteristics of AMEC events captured by MCC. High atmospheric aerosol during dust storm season

increases the AOD and prevents solar insolation signifying a high albedo value. As the albedo increases, temperature decreases at the top of the atmosphere (TOA) creates a favorable condition for the formation of AMEC. Due to adiabatic cooling during deep convection, the water ice parcel reaches a remarkable height in the mesosphere. Initially, the cloud acquires a trapped lee wave structure, and along the tail, the cloud develops propagating lee waves due to high wind speed. Formation temperature at the trough is 180K and in the crest is 200K. A strong wind shear drives the cloud parcel towards the northwestern direction. The cloud's starting point follows the trapped lee wave structure, and the tail part follows the propagating lee wave pattern.

1. Introduction

The appearance of the water ice cloud in the Martian atmosphere is a common phenomenon. Their Spatio-temporal variability is reported from the Mariner era by the scientific community (Wolff et al., 2019; R. Clancy et al., 2017). For the observation of the water ice cloud, scientists adopted so many methods such as orbiting spacecraft, telescopes, and rovers (Curranet al., 1973; Leovy et al., 1973; Herschel et al., 1784; Slipher et al., 1927; Wolff et al., 2005; Anderson and Leovy, 1978; Santer et al., 1986; Jaquin et al., 1986). Marinar-9 television observed some standing waves near-surface of high relief, known as lee wave cloud associated with a surface obstacle (Wildey et al., 1974; Ray et al., 1986; Kahn et al., 1982).

In our present work, we considered the elongated water ice cloud that appears over the Arsia Mons. We note the extended cloud's development with a starting lee wave structure in MCC images in the nadir view. We may also note the tail of AMEC as a separate layer of continuous but non uniform haze over the limb geometry from the past Mars mission. Typically, the detached layer's altitude varies from 40 to 80 km (Anderson and Leovy, 1978; Jaquin et al., 1986, Heavens et al., 2011). This layer is composed of H_2O ice hexagonal crystals. This result was found based on the wavelength-dependent vertical reflectivity profiles with maximum reflection values at red wavelengths, i.e., I/F ~0.2 (Jaquin et al., 1986; Clancy et al., 2007; Smith et al., 2002). Hadley circulation and deep convection help the cloud reach the mesospheric height (Spiga et al., 2013; Havens et al., 2011; Sefton-Nash et al., 2013) to form CO_2 ice, water ice, or dust. Such aerosol distribution was observed by Mars Climate Sounder (MCS) onboard Mars Reconnaissance Orbiter (MRO).

We focus on the unique lee wave structure of the cloud and the characteristics changes in the atmosphere during the appearance of AMEC. Topographic elevation like mountains is involved in AMEC events. While the air parcel passes over the obstacle, it receives a vertical pulse, and then by transforming the potential energy to kinetic energy, the parcel forms a lee wave structure (Durran et al., 1986).

2. Method and Data

We considered the images captured by MCC as our primary data (https://mrbrowse.issdc.gov.in/MOMLTA/protected/browse.xhtml). We processed the raw images using GIMP and MATLAB to enhance the contrast. Since the spatial resolution value varies from pixel to pixel in the image plane, we perform angle and lens correction to the images before the inclusion of the images for scientific observation.

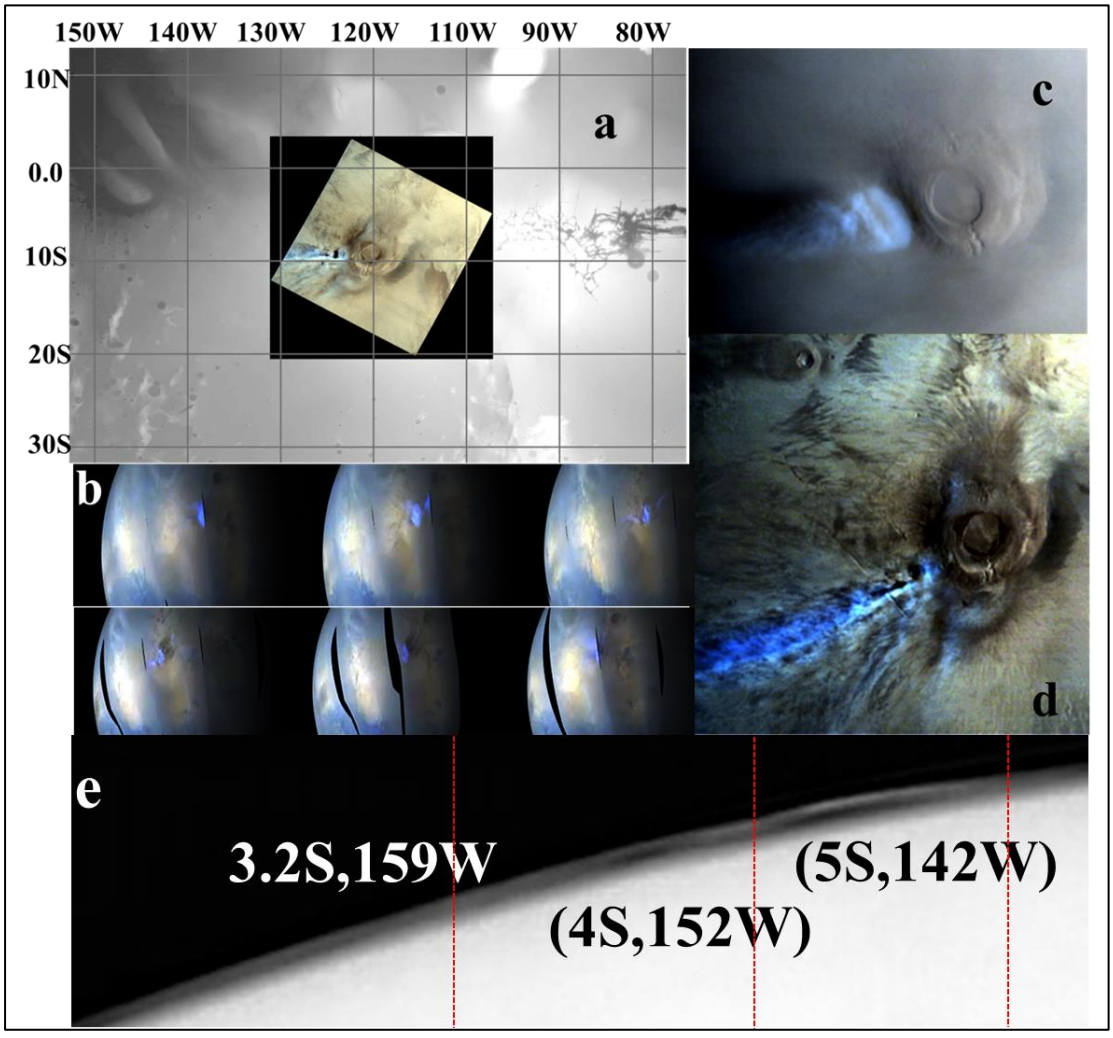

Figure 1. a) Projected MCC image of Arsia Mons over MOLA-DEM. The co-ordinate of the cloud varies from 125 W to 130 W, b) Images captured by MARCI indicating the cloud's appearance as daily phenomena. Global images from 8 Dec 2014 to 13 Dec 2014, c) & d) appearance of the cloud over the slope of Arsia Mons, e) Limb image of the tail following the track mentioned in Bernal et al., 2020.

To achieve the objective of our present work, we first locate Arsia Mons' position by projecting MCC raster images over the MOLA-DEM using ARC-GIS. The location of

the observed area is 120˚W to 130˚W and 0˚ to 10˚ S. Also, we mapped the elevation profile from MOLA-DEM for further analysis with the data available at the following link.

https://planetarymaps.usgs.gov/mosaic/Mars/HRSC_MOLA_Blend/Mars_HRSC_MOLA_BlendShade_Global_200mp_v2.tif

It is difficult to predict the location of the cloud in limb view for two reasons. Firstly, due to the dusty season, and secondly, unavailability of data in the geometry data file. In our case, we processed the geometry file by extrapolating the data to get the exact coordinate for the desired area. In figure 1.e), we may see the processed coordinate for the observed location where the cloud appeared. We processed the .mov file for the MARCI images to get the image frames where Arsia Mons is visible with the daily water ice cloud's appearance. The weather reports may be found at the following link.

http://www.msss.com/msss_images/latest_weather.html

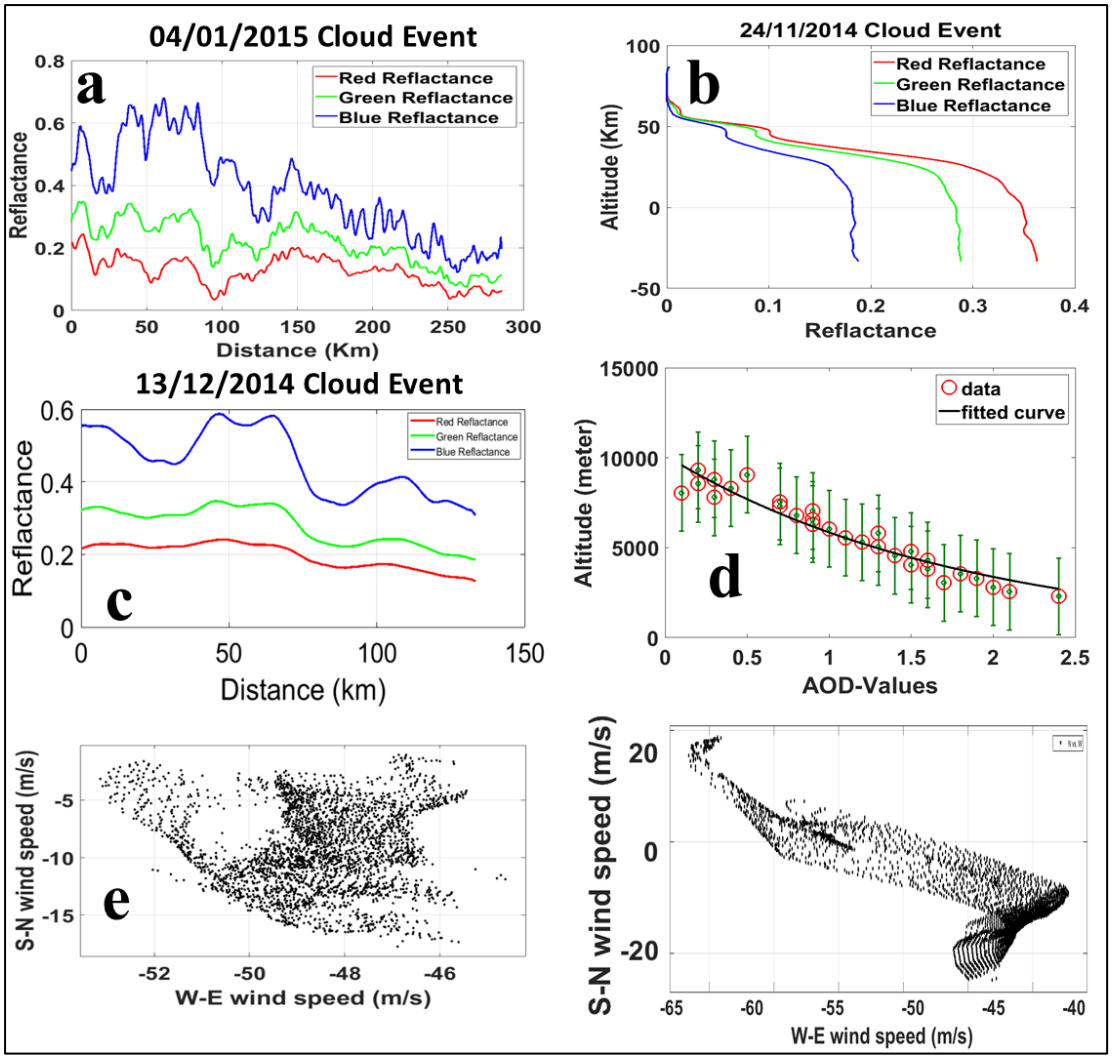

Figure 2. a) Reflectance plot for the event on 04/01/2015. In this image, we see the blue reflectance is more and indicating the presence of water ice cloud b) The presence of water ice cloud above 55 km in the plot representing the limb view of the elongated cloud of Arsia Mons, c) The plot represent the Lee wave structure observed at the starting point of the elongated cloud over the slope of Arsia Mons, d) AOD values over the observed area during the appearance of the cloud, e) & f) We may see the shear during the appearance of the cloud on 4 January 2015 and 13 December 2014.

Further, we developed an algorithm to extract the band data or the DN numbers. DN numbers are the prime requirement to estimate the radiance value of an image. We converted the DN number to radiance and further radiance to reflectance at TOA as follows,

$$Radiance_{\lambda} = \frac{Radiance_{\max_{\lambda}} - Radiance_{\min_{\lambda}}}{QCAL_{\max_{\lambda}} - QCAL_{\min_{\lambda}}} * (QCAL - QCAL_{\min}) + Radiance_{\min_{\lambda}} \quad (1)$$

$$\rho_{\lambda} = \pi * Radiance_{\lambda} * \frac{d^2}{ESUN_{\lambda}} * \cos\theta \quad (2)$$

Where, Radiance λ is the pixel value as radiance, QCAL is the digital number associated with each pixel, Radiance (MIN λ) = spectral radiance scales to QCALMIN Radiance (MAX λ) = spectral radiance scales to QCALMAX, QCALMIN = the minimum quantized calibrated pixel value (typically = 1) QCALMAX = the maximum quantized calibrated pixel value (typically = 255). In the equation 2 ρλ = Planetary reflectance, d = Mars-Sun distance in astronomical units, ESUN λ = mean solar exo-atmospheric irradiances. θs = solar zenith angle. We plotted the reflectance value and the distance in the case of nadir images (figure 2a. and figure 2c.) and altitude for the limb images (figure 2b.). We estimated the wavelength of the cloud from figure 2c. To calculate the wavelength, we adopted the pixel to distance conversion method adopted in Kalita et al., 2021.

We considered a perturbation of (ù+u, w) in the air mass's velocity passes through the high ridge, accompanying the same perturbation for density and pressure. Ganna Valeriyivna Portyankina demonstrated a mathematical formulation to calculate the cloud's wavelength using the wind speed value. We adopted the reverse method for our work to calculate the velocity of the wind. According to the relevant literature, the wavelength of the lee wave cloud is given by (Singh et al., 2018),

$$LW(\lambda) = 2\pi u c_s / g\sqrt{\gamma - 1 - \gamma^2 * u^2 / 4c^2} \quad (3)$$

Where u = wind speed, g= acceleration due to gravity on Mars (3.69 m/s2), LW (λ) = wavelength, γ=Cp/Cv (1.3055), and cs=sound speed for mars~ (226 m/s). Utilizing equation 2.2.1, we estimate the horizontal wind speed that drives the cloud parcel along the northeastern slope of the high ridge topography of Mars. The speed of light

is very high compared to the wind's speed, and hence (such that u2/c2 ≈ 10−3) the third term inside the square root will vanish. We may rearrange the equation as follows (Portyankina et al., 2005),

$$u = gLW(\lambda)\sqrt{(\gamma - 1)} / 2\pi c_s \quad (4)$$

Considering the error in wavelength and Specific heat capacity, we estimated the total error in the calculation of wind speed is ±9.67 m/s. In our present work, estimated wind speed is a bit higher for the Martian atmosphere according to previous wind speed estimates and model results (Mischna et al., 1998; Murphy et al., 1990; Forget et al., 1999).

In the previous studies, researchers calculated the AOD values by contrast variation for the images captured by Viking and HRSC (Forget et al., 1999; Thorpe et al., 1979; Hoekzema et al., 2010 & 2011). We followed the same to estimate the AOD for our observed images. We know that the contrast and the clarification of remote sensing images depend on the atmospheric deposition of water ice and dust particles.

An increment in the AOD makes the surface less visible for observation. Hence, the reflectance at the top of the atmosphere decreases. (Hoekzema et al., 2007, 2010) described the stereo image method based on comparing the contrasts in two HRSC stereo images to estimate atmospheric optical depth over volcano Pavonis Mons (Hoekzema et al., 2007) and Valles Marineris (Hoekzema et al., 2010 & 2011). We briefly describe the stereo method adopted in our present work in the following sections.

Let us consider μ1 and μ2 are the emission angles for two stereo images captured by MCC. If μ1 is greater than μ2, then in association with μ1 has a longer path length through the atmosphere and hence it will show a strong atmospheric contribution in the decrement in contrast as compared to image with emission angle μ2. We may use this difference in comparison to estimate atmospheric optical depth (Appelbaum et al., 1990).

Let us consider the inward radiation to be O (i; j) for the observed image, where indices i, j refer to pixel number for a two-dimensional image. Let R (i; j) represents the upward reflection by the surface in the direction of pixel i, j for the observed image. If we observe without an atmosphere, then O (i; j) and R (i; j) would be equal. However, in the atmosphere on a planet, totally reflected radiation R (i; j) will not reach the camera because of scattering in the atmosphere during its way up through the atmosphere. Therefore, the fraction of R (i; j) that reaches the camera can be written as R (i; j) exp (-τ/μ), where (τ) represent the AOD. In fact, the airborne dust particle scatters only a tiny fraction of incident radiation backward. However, dust haze, water ice, and high altitude cloud haze of microscopic particles significantly

backscatter the incident radiation (Markiewicz et al., 1999; Tomasko et al., 1999). We included the fraction of inbound backscattered radiation and outbound, scattered radiation by the air-born aerosols contributing to the radiation data collected by the Camera by B (i; j). Therefore the radiation at the top of the atmosphere as observed by the camera onboard an Orbiter is given by,

$$O(i,\ j\ ) = R\ (i,\ j)\exp(-\tau / \mu_2) + B(i,\ j) \quad (5)$$

Since B will not show considerable variation over an observed area hence, we may convert the above equation as,

$$contrast(O_1) = (contrast(R_1(i,\ j)\exp(-\tau / \mu_1) \quad (6)$$

$$contrast(O_2) = (contrast(R_2(i,\ j)\exp(-\tau / \mu_2) \quad (7)$$

For a Lambertian surface, R1=R2 for a perfect camera. Therefore, when MCC captures two images with almost similar phase angles, Lambertian approximation is acceptable even with different emission angles. This approximation again considered that the contrast of S1 and S2 would be very similar over a given region while O1 and O2 will be different. In our present study, the phase angle varies from 42.86˚ to 44.69˚ for the stereo images. Now, if we use Lambertian approximation in Eq. 5, we have,

$$contrast(O_1) = \exp(-\tau / \mu_1)(contrast(R_1)\} \quad (8)$$

$$contrast(O_2) = \exp(-\tau / \mu_2)(contrast(R_2)\} \quad (9)$$

Now, the expression of AOD can be written as,

$$\tau = [\mu_1\mu_2 / \mu_1 - \mu_2]\log\{(\ contrast(O_1) / < O_1 >)/(contrast(O_2) / < O_2 >)\}$$

Thus we may estimate the AOD from two stereo images captured by a camera. In figure 2d, we may see the AOD variation as a function of the altitude. Hence we may also find the scale height of AOD and compare it with the pressure scale height to report the nature of the mixture of air and air-born particles.

We consulted MCD-GCM to plot the wind shear. We may see V and U wind's effect along the Tharsis region in figures 2e and 2f.

We know that the Stefan–Boltzmann law can be formulated mathematically as follows (*LoPresto et al*., 2019),

$$L = (\sigma / \pi) * T^4$$
$$=> P = \sigma A T^4 \quad (10)$$

Based on previous literature, we estimated albedo value from the MCC images, and that we used in the modified S-B law and hence we may find the temperature as

$$\Rightarrow T = (1-a)^{1/4} \frac{279}{r^{1/2}} K \qquad 11$$

Where L is the radiance value, σ is Stephen's constant = 5.670367(13) ×10−8 W·m−2·K−4, Where 'T' is the temperature, 'a' denotes albedo value, r is the distance between mars and sun in the atmospheric unit. We took an approach to calculate the albedo value from the direct solar insolation value and the image radiance value. We verified our findings with Mars SWIR Albedo map from Singh et al. (2018) with an error bar of ±.05 K. Estimated temperature varies from 170±3 K to 190±4 K. Further, we re-verified our result with the GCM model and with MCS observed temperature data. We present the temperature and albedo values in figure 4.

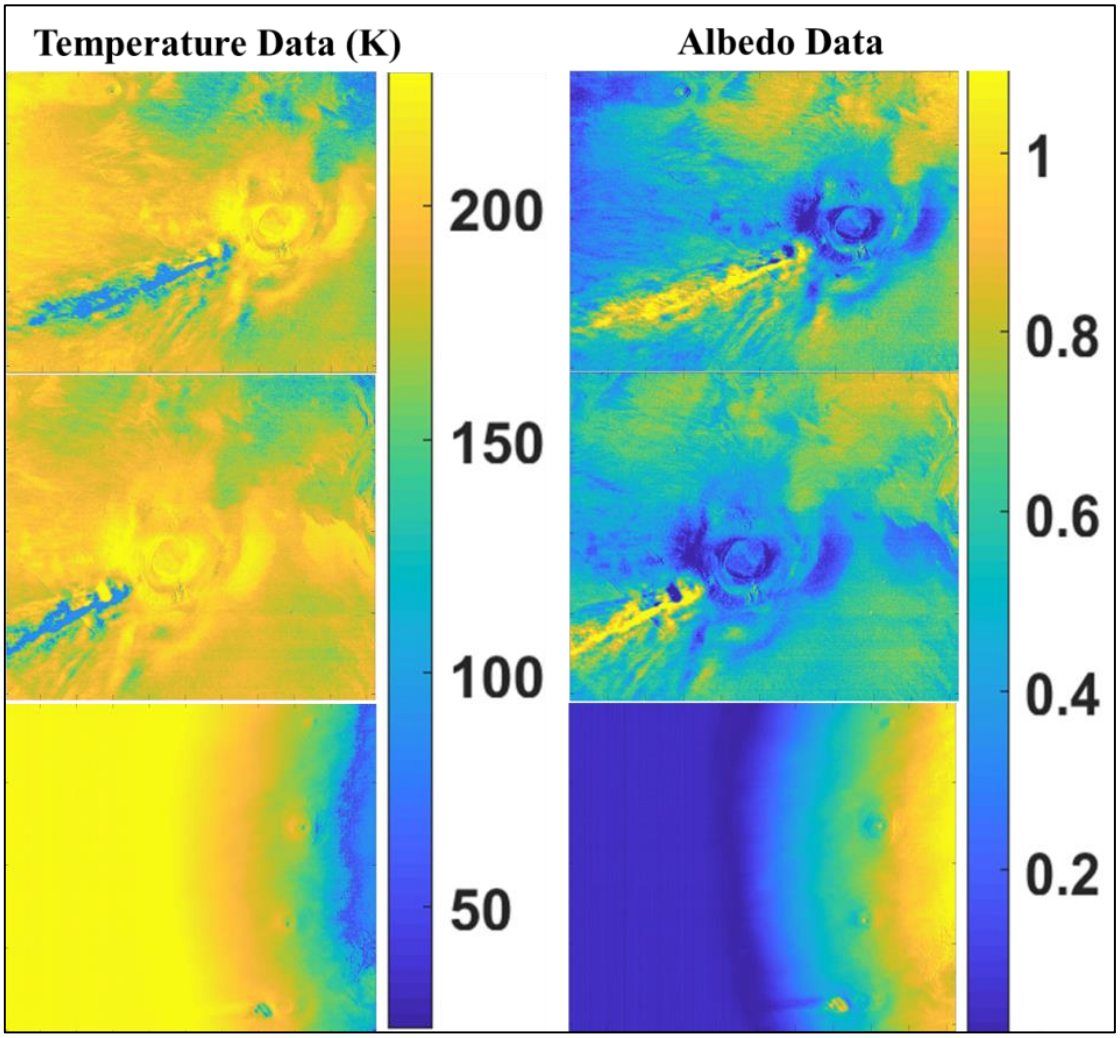

Figure 3. Temperature and Albedo map based on the radiance and reflectance data estimated from the MCC images. a), c) & d) temperature Colour map during 04/01/2015 morning 8:00:00 hr. & 4:00:00 hr. and 13/12/2014 12:00:00. e), f) & g) Albedo color map during 04/01/2015 morning 8:00:00 hr. & 4:00:00 hr. and 13/12/2014 12:00:00.

MRO observe Martian limb, nadir, and off-nadir in nine broadband channels to detect dust, temperature, and condensates (McCleese et al., 2007; Kleinböhl et al., 2009) since September 24, 2006 (LS = 111°, MY 28). We may extract vertical profiles of temperature (K) and water ice extinction (km^{-1}; at 843 cm^{-1} wavenumber) through the limb observations with a moderate (5 km) vertical resolution from the surface to ~80 km altitude through MRO observation (Kleinböhl et al., 2009). The uncertainty in extinction usually varies from 10^{-3} and 10^{-4} km−1 for MRO dust observational data (Benson et al., 2010), whereas the uncertainty in the altitude data varies as ±1 km (Kleinböhl et al., 2009). We used MCS DDR data for MY 33–34 in our present work, available in NASA-PDS. We use the water ice extinction data to analyze the total observed water ice opacity.

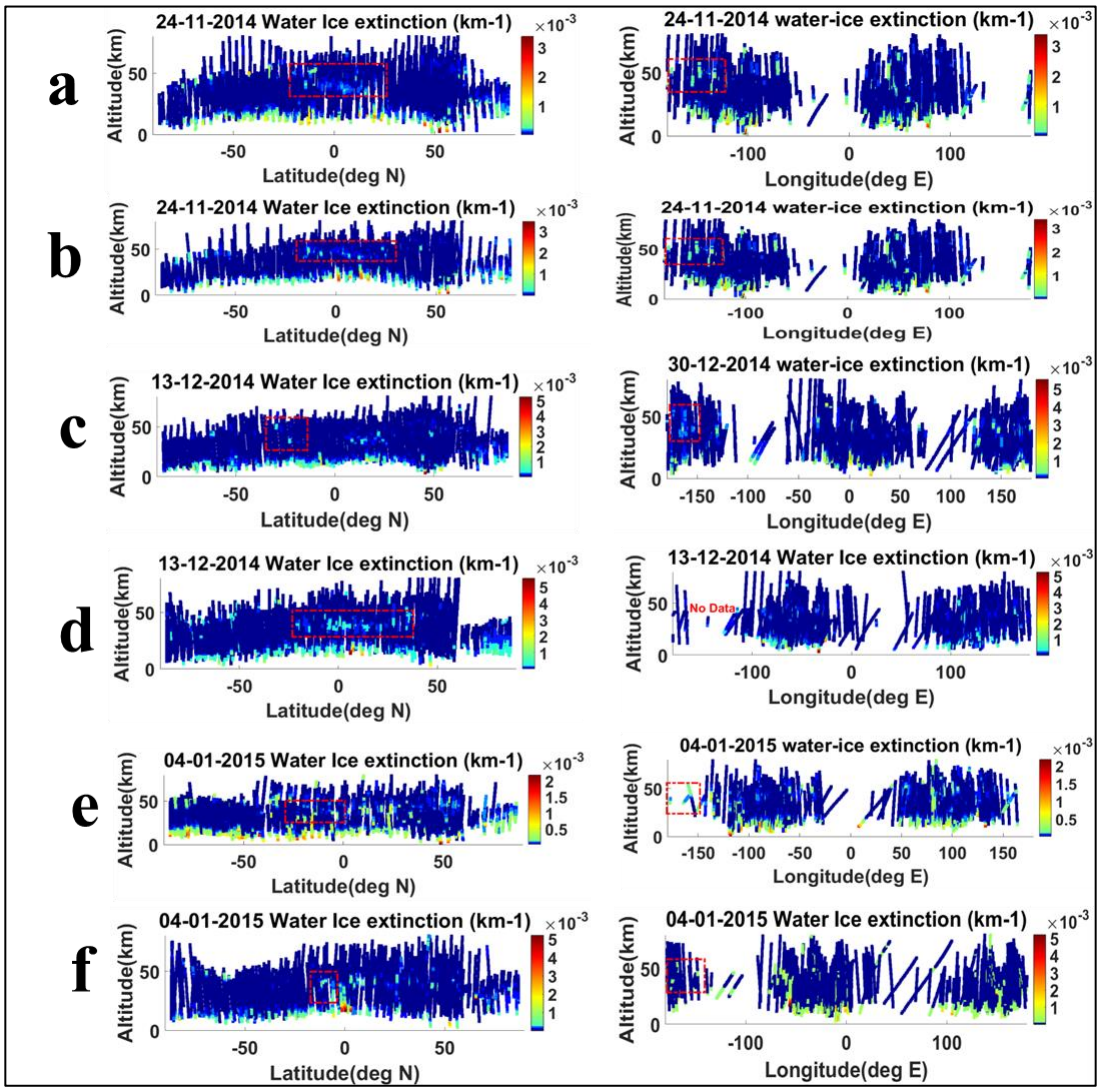

Figure 4. MCS water ice extinction data for the observed event to verify the water ice cloud's presence during the AMEC event. a) & b) Morning and noon (8:00:00 hr. & 12:00:00 hr. 24/11/2014) data is illustrated separately for latitude and longitude as a function of altitude. Red dotted rectangle indicates the presence of water ice for the corresponding event observed through MCC, c) & d) similar illustration for the event on 13/12/2014 during 12:00:00 hr. and 16:00:00 hr. e) & f) similar illustration for the event on 04/01/2015 during 04:00:00 hr. and 08:00:00 hr.

We followed the Mie theory to calculate the radius of the particle. First, we calculate the density scaled opacity derived from MCS dust extinction and water ice extinction data. We used the data to estimate the mixing ratio of water ice particle, then using the Mie theory; we calculated the effective radius of the particle as

$$mixing\ ratio(q) = \frac{4\rho_I(d_z\tau)\,r_{eff}}{3Q_{ext}\rho} \qquad 12$$

The value of *'Qext'* is 0.775, which can be obtained from the Mie theory described by (Kleinböhl et al., 2009) *'reff'* is the effective radius of a dust particle, and density is obtained from MCS data using ideal gas equation. '*ρI'* is the retrieved density that has the value of 900 kg m-3. The effective radius of the dust particle varies from 1.40 to 3.2 μm. The mixing ratio is considered from the MCD GCM for that particular event.

3. Results

We started our study based on the Bernal et al., 2020 that reported the AMEC over Arsia Mons. The initial point of the cloud shows the structure of the lee wave cloud. We already analyzed the lee wave clouds over Ascraeus Mons (Kalita et al., 2021). We may see the same wave structure in 0S/125W image 1c and 4N/135 W 1.d. The calculated wavelength of the largest lee wave cloud varies from 50±2 to 60±3 km. We used the wavelength to estimate the observed area's wind speed and found it to be changing from 71±3.5 m/s to 86±4.9 m/s. Previously reported wind speed was 100 m/s indicates a good consistency with our findings. For the height calculation, we adopted the Brunt-Väisälä frequency method from the previous literature (Durran et al., 1990; Tomasko et al., 1999; Quart and Roy 1949; Ray et al., 1949). We found the height varying from 45±0.3 to 50±0.4 km. We calculated the height based on the limb viewing cloud's pixel counting method and found the height found to be 56±5 km. Our estimation of cloud's height is liaison with the reported height in Bernal et al., 2020.

We estimated the angstrom exponent (α) value based on the observed images' radiance value by adopting the method in previous literature (Mishra et al., 2015; Appelbaum and D J Flood 1989; Kalita et al., 2021). The calculated α value varies from 0.7 to 0.9, indicating coarse mode particle's presence in the cloud portion. We estimated the effective radius of the particle ranges from 1.2 to 3.4μm. During Ls 230 to 260, Mars experiences many dust storms, and the atmosphere becomes hazy due to dust deposition. So we calculated the AOD, which varies from 1.2 to 2.5 over the Arsia Mons slope. We fitted the data exponentially and calculated the scale height of AOD, which comes around 6 to 8 km.

Further, we calculated albedo values for the cloud portion. We found that at the trough, albedo reaches up to the maximum value of 0.8, and in the crest, the albedo value reaches a minimum value of 0.2. The estimated temperature value varies from 170 to 200K. We verified our results with MCD-GCM and MRO-MCS data within 5% of error margin.

4. Discussion

Off-season lee wave structure in the cloud is sporadic during the dust storm season in mars due to flow, high wind speed, and unstable atmosphere. Higher wind

speed and temperature create frequent deep convection activates in the red planet. Hence this rare phenomenon during an off-season catches our attention to study the atmospheric characteristics associated with this event.

During Northern summer in Mars, morning temperature and wind shear are relatively low, which help form such kind of cloud. As we approach the noon, temperature increases and creates pressure differences that supports air parcel to rise to a height of 50km and create favorable conditions for the formation of lee wave cloud. Due to high wind speed and associated atmospheric conditions, adiabatic cooling helps the air parcel to from the cloud.

The resultant velocity of the U and V wind drives the parcel in the northwestern direction. We may clearly notice the cloud's movement in figures 2e, and 2f as a function of the wind shear. As we move further from the Arsia Mons, the wind shear increases drastically and helps expand the cloud. Vertical wind shear also helps the cloud parcel to reach the mesosphere. Our calculated wind speed is higher than that of the model value because the model value was estimated at 45 km as per the reported height in the previous literature (Bernal et al., 2020). On 24/11/2014, MCC captured a high altitude cloud event at 56 km, following the track AMEC as defined in Bernal et al., 2020. So we conclude that along the northwestern part of the Arsia Mons, tail of the AMEC is the high altitude cloud in the images captured by MCC.

We found maximum reflectance in the blue channel indicates the water ice cloud's presence. We verified our finding regarding the presence of water ice cloud with MCS-MRO data. In figure 4, we observe the presence of water ice cloud indicated by the red rectangle. Data duration in MRO-MCS is 4 hours; hence we analyzed two sets of data. One is pre-event, and another is post-event to see the water ice deposition in the atmosphere. Also, we utilize the data to estimate the effective radius of the water ice particle. We consider the mixing ratio constant during the water ice cloud event, and accordingly, we evaluated the particle's radius. From the finding of the present work, it is evident that the effective radius of the water ice particle during dust storm season is higher than that appears during non-dust storm season. During the dust storm season, dust deposition in the Martian atmosphere is maximum, and we may see a higher AOD value. In our present work, we estimated the scale height of AOD to be ~ 7 km which does not match the pressure scale height for the observed period; hence we expect the presence of a heterogeneous mixture at the slope of the Arsia Mons.

The atmospheric temperature and pressure plays a significant role in the dynamics of the planet. So we estimated the cloud's formation temperature. At the slope of Arsia Mons, we may notice a temperature value of 200K, which helps in the cloud's adiabatic transportation to a remarkable height. Crest portion temperature is recorded as 190K. The trough portion temperature is 170K, indicating that the

temperature decreases for the air parcel as it moves upward to the mesosphere. Since we know that maximum albedo means maximum radiation reflecting back to the atmosphere and vice versa, so we estimated our temperature value based on the albedo value. Our estimated albedo vale near-surface matches the finding with previous literature (Singh et al., 2017). For trapped lee wave, cloud condition is favorable near to the slope area. But as we approach along the northwestern track, we may see higher vertical wind shear, and the cloud gains a traveling lee wave structure.

Concluding remarks

In our present work, we analyzed the characteristics of the largest lee wave structure associated with AMEC. We found that due to adiabatic cooling, air parcel rose to the mesosphere and formed the lee wave cloud during the sunrise. As we approached noon, wind speed became high, and the cloud expands at a very high rate. We find maximum AOD during the observed period, and most of the contribution is from water ice cloud over Arsia Mons. Formation temperature for the lee wave cloud is 170K in the trough and 190K in the crest, indicating a deep convection process involve in this off-season phenomenon. We expect to find such lee wave structures as we analyze more MCC images, reveling more interesting features of the Martian atmosphere.

Acknowledgements

The authors are also thankful for the MCC data product team members for providing access to the required data for the present analysis (https://mrbrowse.issdc.gov.in/MOMLTA/) and the Indian Space Research Organization (ISRO) for funding the project with fund reference ISRO/SSPO/MOM-AO/2016-2019. An acknowledgment is due to the Department of Science and Technology for a supporting fund to the Department of Physics, Tripura University, through DST-FIST fund reference SR/FST/PSI191/2014 and also to University Grants Commission SAP fund reference F.530/23/DRS-I/2018(SAP-I).

References

Anderson, E., & Leovy, C. (1978). Mariner 9 Television Limb Observations of Dust and Ice Hazes on Mars. Journal of the Atmospheric Sciences, 35(4), 723–734. https://doi.org/10.1175/1520-0469(1978)035<0723:MTLOOD>2.0.CO;2.

Appelbaum, J., & Flood, D. J. (1990). Solar radiation on Mars. Solar Energy, 45(6), 353–363. https://doi.org/10.1016/0038-092x(90)90156-7.

Benson, J. L., D. M. Kass, A. Kleinböhl, D. J. McCleese, J. T. Schofield, and F. W. Taylor (2010). Mars‟ south polar hood as observed by the Mars Climate Sounder. J. Geophys.Res., https://doi.org/10.1029/2009JE003554

Clancy, R., Montmessin, F., Benson, J., Daerden, F., Colaprete, A., & Wolff, M. (2017). The Atmosphere and Climate of Mars (Cambridge planetary science (pp. 76–105). Cambridge: CambridgeUniversity Press. https://doi.org/10.1017/9781139060172.005i:10.1016/j.icarus.2019.05.041.

Curran, R. J., Conrath, B. J., Hanel, R. A., Kunde, V. G., & Pearl, J. C. (1973). Mars: Mariner 9 Spectroscopic Evidence for H2O Ice Clouds. Science, 182(4110), 381–383. DOI: https://doi.org/10.1126/science.182.4110.381.

Durran, D. R. (1986). Mountain waves. In Mesoscale Meteorology and Forecasting (P. S. Ray, Ed.), pp. 472–492. Am. Meteorol. Soc.

Forget, F., Hourdin, F., Fournier, R., Hourdin, C., Talagrand, O., Collins, M., Huot, J.-P. (1999). Improved general circulation models of the Martian atmosphere from the surface to above 80 km. Journal of Geophysical Research: Planets, 104(E10), 24155–24175. https://doi.org/10.1029/1999je001025.

G. V. Portyankina Dissertation Gottingen (2005).

Heavens, N. G., Kass, D. M., Shirley, J. H., Piqueux, S., & Cantor, B. A. (2019). An Observational Overview of Dusty Deep Convection in Martian Dust Storms. Journal of the Atmospheric Sciences. https://doi.org/10.1175/JAS-D-19-0042.1.

Hernández Bernal, Jorge & Sánchez‐Lavega, A. & Río-Gaztelurrutia, T. & Ravanis, Eleni & Cardesin-Moinelo, Alejandro & Connour, K. & Tirsch, Daniela & Ordóñez Etxeberria, Iñaki & Gondet, B. & Wood, S. & Titov, D. & Schneider, N. & Hueso, R. & Jaumann, R. & Hauber, E.. (2020). An Extremely Elongated Cloud over Arsia Mons Volcano on Mars: I. Life Cycle. Journal of Geophysical Research: Planets. 126. https://doi.org/10.1029/2020JE006517.

Herschel, W. (1784). On the remarkable appearance of the polar regions of the planet Mars, the inclination of its axis, the position of its poles, and its spheroidal figure; with a few hints relating to its real diameter and its atmosphere. Philosophical Transactions of the Royal Society of London, 24, 233–273.

Hoekzema, N. M., Garcia-Comas, M., Stenzel, O. J., Grieger, B., Markiewicz, W. J., Gwinner, K., & Keller, H. U. (2010). Optical depth and its scale-height in Valles Marineris from HRSC stereo images. Earth and Planetary Science Letters, 294(3-4), 534–540. https://doi.org/10.1016/j.epsl.2010.02.009.

Hoekzema, N. M., Garcia-Comas, M., Stenzel, O. J., Petrova, E. V., Thomas, N., Markiewicz, W. J., Delamere, W. A. (2011). Retrieving optical depth from shadows in orbiter images of Mars. Icarus, 214(2), 447–461. https://doi.org/10.1016/j.icarus.2011.06.009.

Hoekzema, N.M., Garcia Comas, M., Gwinner, K., Grieger, B., Markiewicz, W.J., Keller, H.U., (2007). The Scale-Height of Dust Around Pavonis Mons from HRSC Stereo Images. Seventh International Conference on Mars, LPI Contributions No. 1353, p. 3154.
https://www.mps.mpg.de/phd/theses/atmosphere-surface-vapor-exchange-and-ices-in-the-martian-polar-regions.pdf.

Jaquin, F., Gierasch, P., & Kahn, R. (1986). The vertical structure of limb hazes in the Martian atmosphere. Icarus, 68(3), 442–461.

Kahn, R., & Gierasch, P. (1982). Long cloud observations on Mars and implications for boundary layer characteristics over slopes. Journal of Geophysical Research, 87(A2), 867 https://doi.org/10.1029/JA087iA02p00867.

Kalita, J., Mishra, M.K. & Guha, A. (2021). Martian Lee-wave cloud near Ascraeus Mons during Martian years 33 and 34: a study based on the Mars color camera (MCC) images. Indian J Phys. https://doi.org/10.1007/s12648-020-01978-y.

Kleinböhl, A., (2009). Mars Climate Sounder limb profile retrieval of atmospheric temperature, pressure, dust, and water ice opacity, J. Geophys. Res., 114, E10006, https://doi.org/10.1029/2009JE003358.

Leovy, C. B., Briggs, G. A., & Smith, B. A. (1973). Mars atmosphere during the Mariner 9 extended mission: Television results. Journal of Geophysical Research, 78(20), 4252–4266. https://doi.org/10.1029/JB078i020p04252.

LoPresto, M. C. (2019). Estimating the temperatures of possibly habitable extrasolar planets. The Physics Teacher, 57(8), 568–569. https://doi.org/10.1119/1.5131135.

Markiewicz, W. J., Sablotny, R. M., Keller, H. U., Thomas, N., Titov, D., & Smith, P. H. (1999). Optical properties of the Martian aerosols as derived from Imager for Mars Pathfinder midday sky brightness data. Journal of Geophysical Research: Planets, 104(E4), 9009–9017. https://doi.org/10.1029/1998je900033.

McCleese, D. J., (2007). Mars Climate Sounder: An investigation of thermal and water vapor structure, dust and condensate distributions in the atmosphere, and energy balance of the polar regions, J. Geophys. Res., 112, E05S06, https://doi.org/10.1029/2006JE002790.

Mischna, M., J.F. Bell III, P.B. James., D. Crisp., (1998). Synoptic measurements of Martian winds using the Hubble Space Telescope, Geophys. Res. Lett., 25, 611-614, https://doi.org/10.1029/98GL50358.

Mishra, M. K., Chauhan, P., Singh, R., Moorthi, S.M., Sarkar, S.S. (2016). Estimation of dust variability and scale height of Atmospheric Optical Depth (AOD) in the Valles Marineris on Mars by Indian Mars Orbiter Mission (MOM) data. Icarus, 265, 84-94. https://doi.org/10.1016/j.icarus.2015.10.017.

Murphy, J.R., Pollack, J.B., Haberle, R.M., Leovy, C.B., Toon, O.B., Schaeffer, J. (1990). Three-dimensional numerical simulation of Martian global dust storms. Journal of Geophysical Research. 100: 26,357-26,376.

Ray, P. S. (Ed.). (1986). Mesoscale Meteorology and Forecasting. https://doi.org/10.1007/978-1-935704-20-1.

Santer, R. & Deschamps, M. & Ksanfomality, L. & Dollfus, A.. (1986). Photopolarimetry of Martian Aerosols: II. Limb and Terminator Measurements. Astronomy and Astrophysics. 158. 247-258.

Sefton-Nash, E., Teanby, N. A., Montabone, L., Irwin, P. G. J., Hurley, J., & Calcutt, S. B. (2013). Climatology and first-order composition estimates of mesospheric clouds from Mars Climate Sounder limb spectra. Icarus, 222(1), 342–356. https://doi.org/10.1016/j.icarus.2012.11.012.

Singh, R. & Chauhan, P. (2018). Lee Wave Clouds in the Mars Colour Camera (MCC) Images: Wind Speed Measurements.

Slipher, E. (1927). Atmospheric and Surface Phenomena on Mars. Publications of the Astronomical Society of the Pacific, 39(230), 209-216. Retrieved March 27, 2021, from http://www.jstor.org/stable/40692693.

Smith, M.D., 2002. The annual cycle of water vapor on Mars as observed by the thermal emission spectrometer. J. Geophys. Res. 107, 5115, https://doi.org/10.1029/2001JE001522.

Thorpe, T. E. (1979). A history of Mars atmospheric opacity in the Southern Hemisphere during the Viking extended mission. Journal of Geophysical Research, 84(A11), 6663. https://doi.org/10.1029/ja084ia11p06663.

Tomasko, M. G., Doose, L. R., Lemmon, M., Smith, P. H., & Wegryn, E. (1999). Properties of dust in the Martian atmosphere from the Imager on Mars Pathfinder. Journal of Geophysical Research: Planets, 104(E4), 8987–9007. https://doi.org/10.1029/1998je900016.

WILDEY, R. (1974). Martian lee waves revisited. Nature 249, 132–133. https://doi.org/10.1038/249132a0.

Wolff, M. J., Clancy, R. T., Banfield, D., & Cuozzo, K. (2005). Water ice clouds as seen from the Mars Exploration Rovers. AGU fall meeting abstracts.

Wolff, M. J., Clancy, R. T., Kahre, M. A., Haberle, R. M., Forget, F., Cantor, B. A., & Malin, M. C. (2019). Mapping Water Ice Clouds on Mars with MRO/MARCI. Icarus. https://doi.org/10.1016/j.icarus.2019.05.041.

Figure_1.

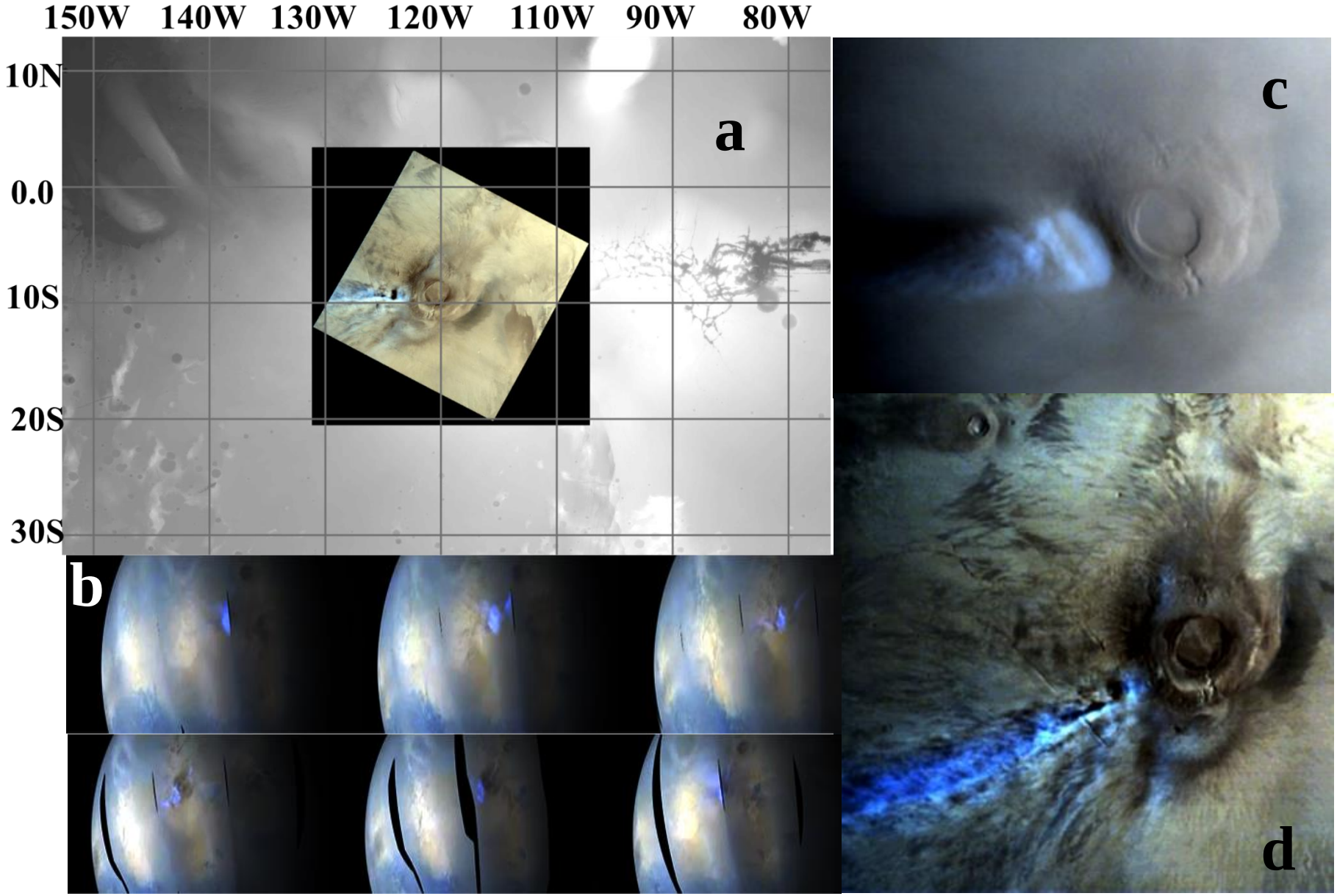
150W
140W
130W
120W
110W
90W
80W
10N
0.0
10S
20S
30S
a
b
c
d

Figure_2.

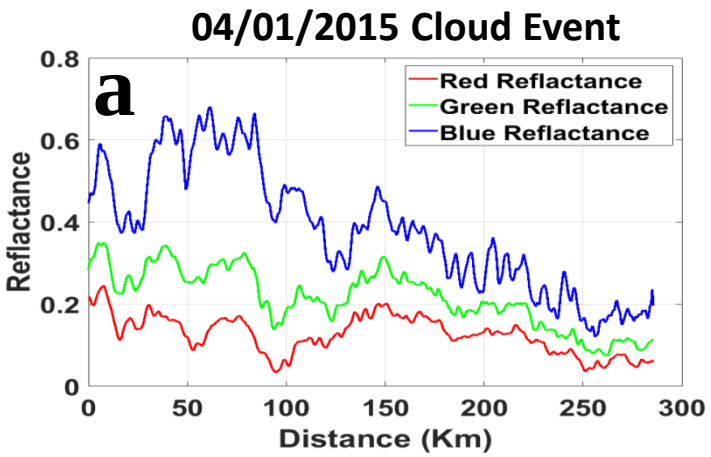
04/01/2015 Cloud Event
a
Red Reflactance
Green Reflactance
Blue Reflactance
Reflactance
Distance (Km)

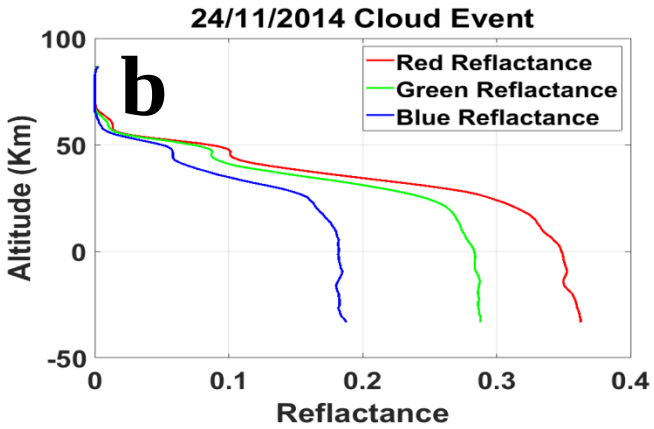
24/11/2014 Cloud Event
b
Red Reflactance
Green Reflactance
Blue Reflactance
Altitude (Km)
Reflactance

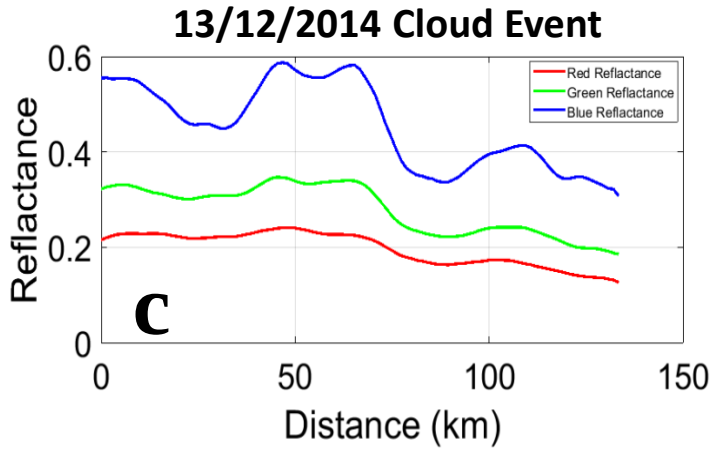
13/12/2014 Cloud Event
c
Red Reflactance
Green Reflactance
Blue Reflactance
Reflactance
Distance (km)

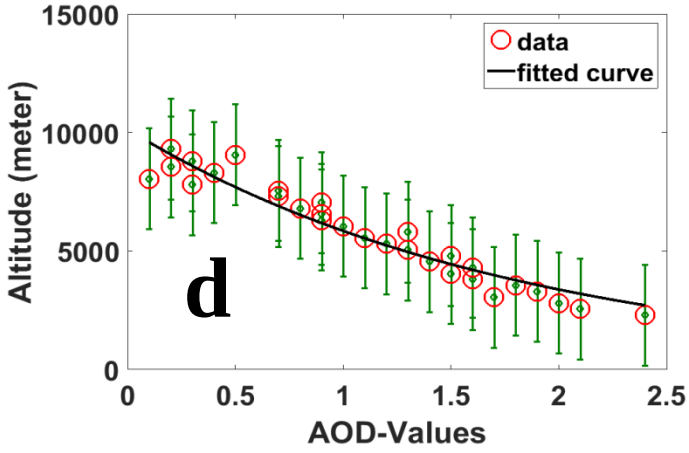
d
data
fitted curve
Altitude (meter)
AOD-Values

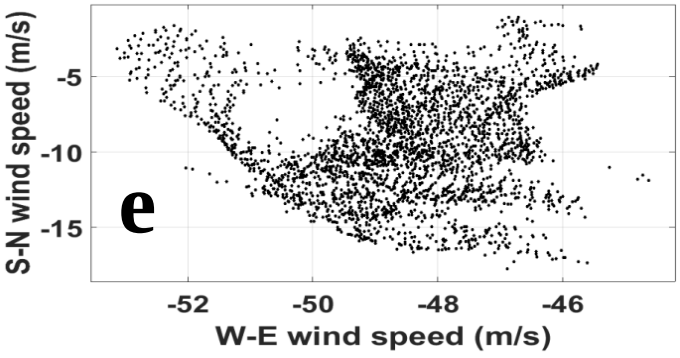
e
S-N wind speed (m/s)
W-E wind speed (m/s)

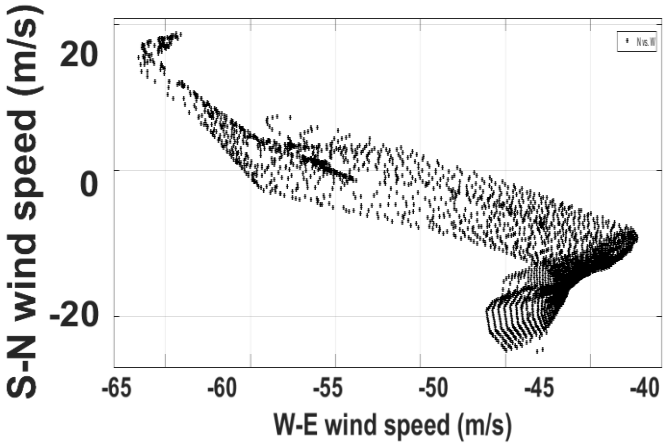
S-N wind speed (m/s)
W-E wind speed (m/s)

Figure_3.

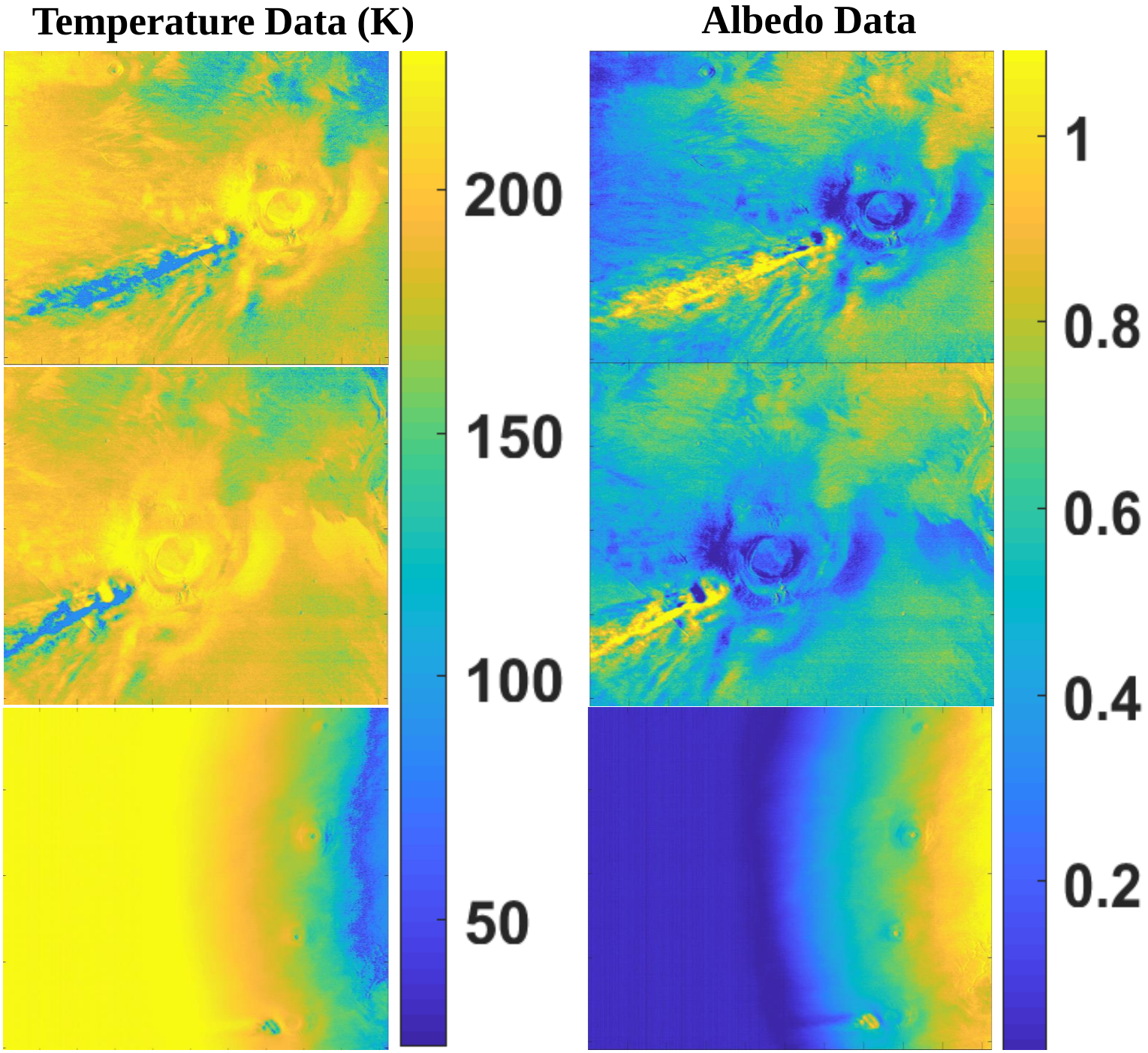
Temperature Data (K)
Albedo Data
200
150
100
50
1
0.8
0.6
0.4
0.2

Figure_4.

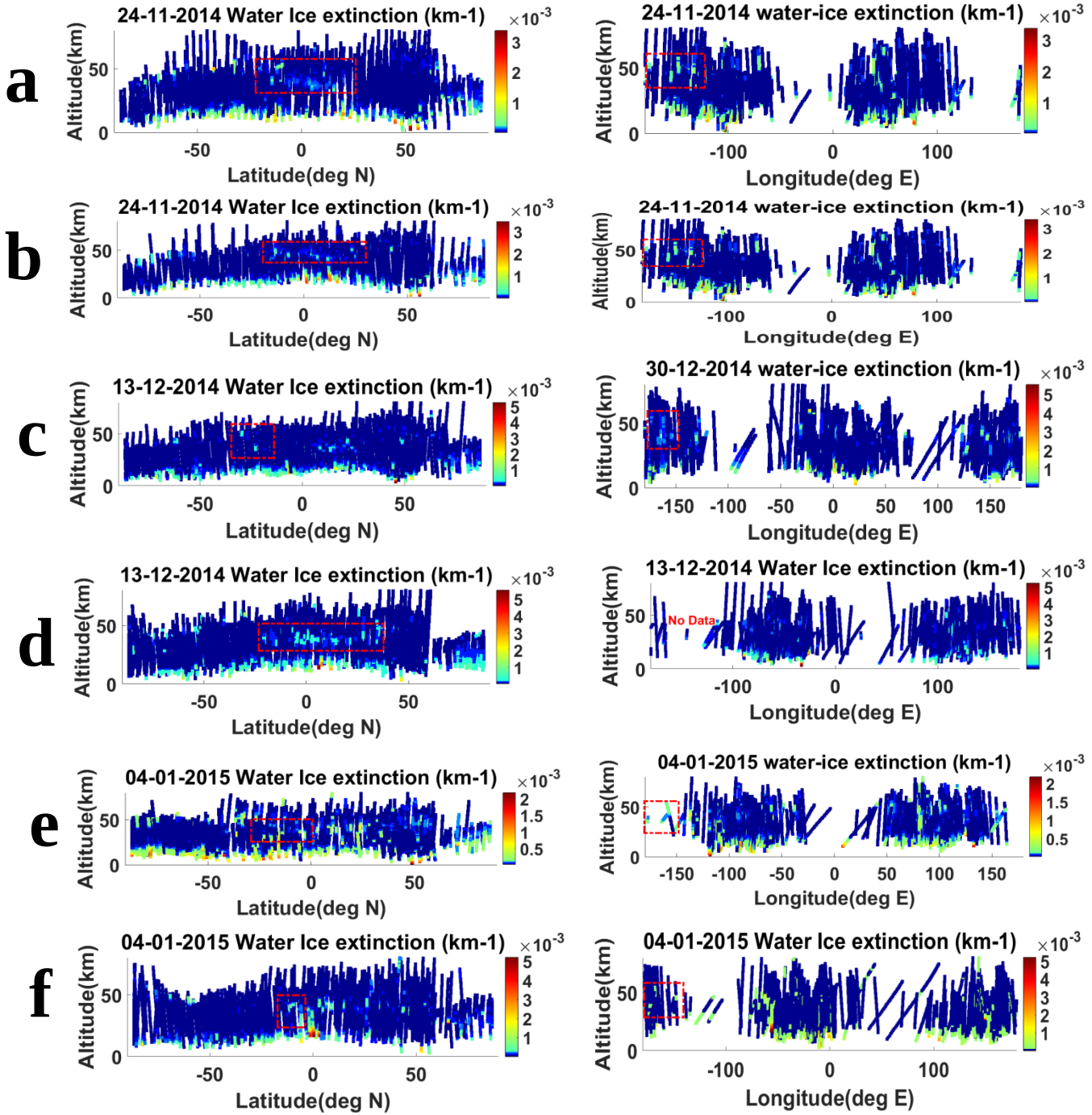
a
24-11-2014 Water Ice extinction (km-1)
24-11-2014 water-ice extinction (km-1)
b
24-11-2014 Water Ice extinction (km-1)
24-11-2014 water-ice extinction (km-1)
c
13-12-2014 Water Ice extinction (km-1)
30-12-2014 water-ice extinction (km-1)
d
13-12-2014 Water Ice extinction (km-1)
13-12-2014 Water Ice extinction (km-1)
No Data
e
04-01-2015 Water Ice extinction (km-1)
04-01-2015 water-ice extinction (km-1)
f
04-01-2015 Water Ice extinction (km-1)
04-01-2015 Water Ice extinction (km-1)
Altitude(km)
Latitude(deg N)
Longitude(deg E)
×10-3